DFT study of Atomic and electronic structures of *trans*-vacant 1*M* Al-rich illite

Wei Gao[1,2], Jian Zhao[1,2,*], Man-Chao He[1,2]

[1] State Key Laboratory of Geomechanics and Deep Underground Engineering, China University of Mining and Technology, Beijing 100083, China

[2] School of Mechanics and Civil Engineering, China University of Mining and Technology-Beijing, Beijing 100083, China

*E-mail address of corresponding author: zhaojian@cumtb.edu.cn

Abstract- Illite is a common clay mineral that is found in a wide range of geological settings. The good thermal stability and non-swelling properties of illite make it valuable in ceramic materials, paints and coatings, drilling fluids, agriculture, and geologic studies. To gain a deeper understanding of the physical and chemical properties of illite, in the present paper, the atomic and electronic structures of a typical *trans*-vacant 1*M* Al-rich illite were constructed and calculated by density functional theory (DFT). The calculated indirect band gap of Al-rich illite was 4.99 eV. The electronic analysis revealed that the interactions in tetrahedron sheet were more stable than those in octahedral sheet. The substitution of Al atoms noticeably reduced the stability of the tetrahedral sheet in Al-rich illite. Other properties of Al-rich illite, including the density of states, electron population/charge, electronic charge density and bonding interaction were also discussed and analyzed in detail.

Keywords- Al-rich illite, Clay Minerals, Crystal structures, DFT Calculations.

1. Introduction

Illite is a type of mica-like phyllosilicate clay mineral. The name was introduced by Grim (Grim *et al.*, 1937) and derived from the name of the state of Illinois, USA. Illite is a widespread mineral found in diverse geological environments, primarily originating from the weathering and alteration of other minerals like micas and feldspars (Righi & Meunier, 1995; Shoval,

Mineralogical Society

This is a 'preproof' accepted article for Clay Minerals. This version may be subject to change during the production process.
DOI: 10.1180/clm.2023.35

2023). The good thermal stability (He *et al.*, 1995) and non-swelling properties (Ruiz Pestana *et al.*, 2017) of illite make it valuable in a wide range of industrial and geological applications, including ceramic materials, paints and coatings, drilling fluids, agriculture, and geologic studies (Steiger, 1982; Feng *et al.*, 1999; Sedmale *et al.*, 2017; Li *et al.*, 2018; Zhang *et al.*, 2020; El Halim *et al.*, 2022).

Existing experimental and theoretical data have confirmed the 2:1 type dioctahedral layered structure of illite, which consists of stacked layers primarily bound by van der Waals forces (Brigatti & Guggenheim, 2002). An individual 2:1 basic layer comprises two tetrahedral sheets sandwiching one octahedral sheet to form a T–O–T structure (Bergaya & Lagaly, 2013). The tetrahedral sheets are composed of Si–O tetrahedrons with some of the Si atoms substituted by Al atoms, while the octahedral sheet consists of Al, Mg, or Fe cations coordinated with OH groups (Meunier & Velde, 2004). The interlayer space of illite primarily accommodates K ions, and the interlayer charge generally ranges between 0.6 and 0.85 per $O_{10}(OH)_2$ (Rieder *et al.*, 1998). The octahedral sheet of illite exhibits two types of structure, *cis*-vacant and *trans*-vacant, which were determined by the configuration of coordinating OH groups (Drits *et al.*, 2006; Drits *et al.*, 2012). In terms of

2

polytypes, it has been observed that the $1M$ and $2M_l$ polytypes are the most frequently encountered in illite species (Zoeller & Brockamp, 1997; Zviagina & Drits, 2019).

Due to the complexity of the chemical component, disordered stacking, cation substitutions, cation configurations and small crystalline domain size of illite, accurately measuring its atomic structure and crystal properties through experiments remains challenging. With advancements in theoretical research, computational chemistry calculations based on DFT have been proven to be an effective and reliable tool for investigating clay minerals at the molecular level (Bridgeman, 1996; Beermann & Brockamp, 2005; Mercier *et al.*, 2010; He *et al.*, 2012; Teich-McGoldrick *et al.*, 2012; Scholtzová & Tunega, 2019; Yuan *et al.*, 2022; Zhao *et al.*, 2023). A series of works have been published on the investigations of illite structure by DFT. Stixrude & Peacor (2002) discussed two avaliably competing models in illite–smectite system based on first-principles study. The result revealed the fact that differences in energy and structure between the two models can be understood in terms of local charge balance. Militzer *et al.* (2011) calculated the elastic constants of muscovite illite-smectite by DFT theory, the difference indicated the variations in their crystal sturctures. Geatches & Wilcox (2014)

modeled a variety of interlayer-deficient dioctahedral mica models of the 1M-illite series based on crystallographic data and average formulae with DFT, and analyzed the differences between *cv/tv* models. Escamilla-Roa *et al.* (2016) investiaged the stability of the hydronium cation in the structure of illite. The results revealed hydronium cation remains in the interlayer of illite at a higher temperacture. Sánchez-Coronilla *et al.* (2019) investigated the inclusion of Fe, Cu, and Zn in Illite. After analysed the stability and electronic effect of the inclusion system, illite presented a good adsorption characteristic of Fe, Cu, and Zn in the (1, 0, 0) site.

In the present paper, a DFT study of a typical *trans*-vacant 1*M* Al-rich illite without octahedral substitution is reported by calculating its atomic and electronic structure, density of states (DOS), electron population/charge, electronic charge density, and bonding interaction analysis. The current DFT results will contribute to a better understanding of the chemical, physical, and mechanical properties of illite from a microscopic perspective.

2. Method of calculations

The periodic DFT calculations were conducted with the Vienna *ab initio* simulation package (VASP) (Monkhorst & Pack, 1976; Kresse & Furthmüller, 1996). The interaction between the ions and valence electrons is described by

4

the full-potential frozen-core all-electron projector augmented wave (PAW) method proposed by Blöchl. (Blöchl, 1994; Kresse & Joubert, 1999). Plane-wave pseudopotentials and periodic boundary conditions were applied when solving the Kohn-Sham DFT equations. The electron exchange potential and correlation energy were calculated using the Perdew-Burke-Ernzerhof (PBE) form of the generalized gradient approximation (GGA) (Perdew *et al.*, 1996). In the present paper, a (3×4×3) Monkhorst-Pack k-point was utilized for Brillouin zone integrations. The corresponding plane-wave basis cutoff energy was set at 450 eV. Geometry optimization was terminated when the Hellman-Feynman forces acting on each atom fell below 0.01 eV/Å, and the self-consistency iterations concluded once the total energies converged to within 10^{-4} eV. The valence electron configurations of the elements in Al-rich illite were determined to be H $1s^1$, O $2s^22p^4$, Al $3s^23p^1$, Si $3s^23p^2$, and K $3s^23p^64s^1$. The accuracy of calculations for weak interactions was ensured by employing the DFT-D3 dispersion correction method (Moellmann & Grimme, 2014).

The Mulliken population/charges calculations and crystal orbital Hamilton population (COHP) bonding analyses were conducted by the LOBSTER package. (Hughbanks & Hoffmann, 1983; Dronskowski &

5

Bloechl, 1993; Maintz *et al.*, 2016; Ertural *et al.*, 2019). Basis sets given by Koga and S. Maintz which fitted to atomic VASP GGA-PBE wave functions were employed during the projection (Koga *et al.*, 2000).

3. Results and Discussion

The system of $K_xAl_2(Si_{4-x}Al_x)O_{10}(OH)_2$ was considered to determine the chemical formula of Al-rich illite, where $x = 0.6 \sim 0.85$ to conform the required layer charge and lattice substitution ratio. Based on the chemical composition analysis of Al-rich illite samples (Drits *et al.*, 2010), in the present paper, $x = 0.75$ for the ideal chemical formula of $K_{0.75}Al_2(Si_{3.25}Al_{0.75})O_{10}(OH)_2$ was selected to represent a type of Al-rich illite. The initial cell configuration of the Al-rich illite was derived from the illite cells constructed by Drits (Drits *et al.*, 2010) and consisted of a *trans*-vacant dioctahedral 1*M* polytype structure. K ions were introduced in the interlayer to balance the cell charge. Subsequently, Si atoms in the silica-oxygen tetrahedrons were substituted with Al atoms to afford the $K_3Al_8(Si_{13}Al_3)O_{40}(OH)_8$ chemical formula. The configurations of the 3 substituted tetrahedral Al atoms were comprehensively analyzed through calculations, as presented in Table 1. To provide a clearer and more intuitive demonstration, a selection of representative configurations was chosen and

6

presented (arranged in order of energy) in Fig. 1. Lower energy corresponds to a more stable structure. The results revealed that the local aggregation of Al–O tetrahedrons results in reduced stability of Al-rich illite cell, which was related to the partial local balance between the interlayer charge and the charge-deficient tetrahedral sheets (Stixrude & Peacor, 2002).

The final optimized crystal structure model of Al-rich illite (with the most stable configuration of substituted tetrahedral Al atoms) was presented in Fig. 2(a). The calculated structural parameters were: $2a$ = 10.454 Å, b = 9.021 Å, c = 10.316 Å, α = 89.93°, β = 101.99°, and γ = 89.92°, which were in good agreement with the existing experimental data (Eberl *et al.*, 1987; Drits & McCarty, 2007), as shown in Table 2. The major bond lengths of Al-rich illite were presented in Table 3. Considering the difference in symmetries and positions, as marked in Fig. 2(b), the Al atoms were divided into two kinds: Al_a was an Al atom in octahedral sheet; Al_b was a substituted Al atom in tetrahedral sheet. The O atoms were divided into five kinds: O_a was an O atom of the hydroxyl in octahedral sheet; O_b was an inner O atom shared by Si–O tetrahedron and Al–O octahedron; O_c was an inner O atom shared by Al–O tetrahedron and Al–O octahedron; O_d was an O atom in tetrahedral sheet connected between Si and

7

Al_b; O_e was an O atom in tetrahedral sheet connected between Si atoms. The result revealed that the length of the bonds in octahedral sheet (Al_a–O_a, Al_a–O_b and Al_a–O_c) were all longer than that of the bonds in tetrahedral sheet (Si–O_b, Al_b–O_c, Si–O_e, Al_b–O_d and Si–O_d), which implied that the bonding interactions in octahedral sheet were weaker than those in tetrahedral sheet. The length of the bonds in Si–O tetrahedron (Si–O_e, Si–O_b and Si–O_d) were all shorter than that of the bonds in Al–O tetrahedron (Al_b–O_c and Al_b–O_d), which indicated that the substitution of Al atom reduced the connection strength of tetrahedral sheet.

Fig. 3 displayed the band structure of Al-rich illite near the Fermi level. The high-symmetry Brillouin zone points were G(0,0,0), F(0,0.5,0), Q(0,0.5,0.5), and Z(0,0,0.5). The conduction-band minimum (CBM) of Al-rich illite is at the G point and the valence-band maximum (VBM) is at the F point. Thus, Al-rich illite was calculated to have an indirect band gap with a gap width of 4.99 eV. This characteristic illustrated that Al-rich illite can be treated as insulator.

To further investigate the electronic properties of Al-rich illite, the electronic total density of state (TDOS) and electronic partial density of state (PDOS) for H, O, Al, Si, and K atoms were calculated and presented in Fig.

8

4. Five types of O atoms and two types of Al atoms were individually plotted, taking into account their symmetries and positions. The Fermi energy has been set at zero. The TDOS within the energy range of -35 to 0 eV exhibited four prominent peaks, labeled as 1 ~ 4 in Fig. 4(a) or (a'). It was obvious that peaks 1 and 3 were solely contributed by the K s and p states. Peak 2 was mainly from the O $2s$ states, with a partially contribution of Si and Al $3s/3p$ and H $1s$ states. In contrast, peak 4 was almost entirely contributed by the $2p$ states of O atoms. Integrating the band structures in Fig. 3, it became evident that the top of valence-band is primarily composed of the $2p$ states of O atoms, while the bottom of conduction-band includes the $3s/3p$ states of Si and Al atoms. Five different types of O atoms exhibited similar PDOS curves, which were attribute to the high ionicity of the oxygen, resulting in charge transfer from adjacent H, Al, and Si atoms. As shown in Figs. 4(b), (c), and (g), the overlap between O_b $2s$ state and H $1s$ state split into two peaks due to the hybridization with Al_a $3s/3p$ states in octahedral sheet. Similarly, a particular narrow peak of O $1s$ state arose in the PDOS plot of O_c (Fig 4(c)), which contributed the peak 2' of the TDOS plot. In tetrahedral sheet, as shown in Figs. 4(d), (e), (h), (i), (j), and (k), the substituted Al_b atom presented a different hybrid mode with adjacent O atoms compared to the Si atom. It was

9

obvious that the degree of hybridization between Si $3p$ state and adjacent O $2p$ state was stronger than that between Al_b $3p$ state and adjacent O $2p$ state.

The atomic Mulliken population/charges analysis and the crystal orbital Hamilton population (COHP) bonding analysis for characteristic atoms and bonds in Al-rich illite were implemented with the LOBSTER package and summarized in Table 4. The Mulliken charge populations provide a comprehensive quantification of the charge transfers occurring within the crystals. The result revealed that five types of O atoms gained $0.96 \sim 1.16$ e, while the adjacent K lost 1.01 e, H lost 0.42 e, Si lost 2.18 e, Al_b lost 1.73 e, and Al_a lost 1.62 e. In tetrahedral sheet, Si atom lost more electrons than substituted Al_b atom, which indicated a stronger charge transfer between Si atom and adjacent O atoms. Moreover, the residual electrons in Al $3s/3p$ and Si $3s/3p$ states revealed the covalent character of Si–O and Al–O bonds in tetrahedrons and octahedrons. COHP can reveal the nature of covalent interactions between bonding atoms, while the integrated COHP (ICOHP) values up to the Fermi level yields are the bond contributions to the band-structure energy what hints towards the bond strength. The calculated ICOHP values of bonds Al_a–O_a, Al_a–O_b, Si–O_b, Al_b–O_c, Si–O_e, Al_b–O_d, and Si–O_d were -4.17, -3.96, -7.63, -5.47, -7.63, -5.83, and -8.36 eV, respectively,

10

indicating that the bonding interaction strength of these bonds followed the order $Si–O_d > Si–O_b > Si–O_e > Al_b–O_d > Al_b–O_c > Al_a–O_a > Al_a–O_b$. The results revealed that, in tetrahedral sheet, Si–O bonds were significantly stronger than Al–O bonds, suggesting that the substitution of Al_b weakened the stability of the silica tetrahedrons. On the other hand, Si–O and Al–O bonds in tetrahedral sheet were all stronger than Al–O in octahedral sheet, indicating that tetrahedral sheet was more stable than octahedral sheet even in the presence of substitution.

To gain a more intuitive understanding of the bonding properties and charge distribution of atoms in the tetrahedral sheet of Al-rich illite, the 3D and 2D electronic charge density contour plots (Fig. 5) were sampled within the plane containing the Si, Al_b, and O_d atoms, which were positioned at the center of the diagram. To better observe the charge density variation between atoms, regions with electronic charge density exceeding $1\ e\ /\ Å^3$ were colored in white. The results revealed that the charge density around the O_d was substantial, indicating the high electronegativity of the O atom. The overlap of charge density within the $Si–O_d$ and $Al_b–O_d$ bond regions indicated covalent bonding properties. The dense contour lines within the $Si–O_d$ bond region implied a stronger covalent bonding interaction compared to $Al_b–O_d$

11

bond, which was consistent with the conclusions above. Furthermore, the sparse contour lines around Al_b atom revealed an ionic bonding characteristic of Al_b–O_d bond. This mixed ionic/covalent bonding property has also been discovered in other clay minerals such as kaolinite and montmorillonite.

Further crystal orbital Hamilton population (COHP) analyses including main orbital-pair contributions were performed to investigate the bonding interactions of Si–O_d, Al_b–O_d and Al_a–O_b, as shown in Fig. 6. A comparison of Si–O_d bond (ICOHP = −8.36 eV) and Al_b–O_d bond (ICOHP = −5.83 eV) in tetrahedral sheet (Fig. 6(a) and (b)) revealed that all the interactions ($3s$–$2s$, $3s$–$2p$, $3p$–$2s$, and $3p$–$2p$) of Si–O_d bond were enhanced compared to Al_b–O_d bond. Particularly noteworthy was the $3p$–$2p$ orbital-pair (ICOHP = −2.94 eV), which reached a similar characteristic strength level as the $3p$–$2s$ orbital-pair (ICOHP = −2.95 eV). The result revealed a high degree of hybridization between orbitals of Si and O_d atoms, especially the Si $3p$ state and O_d $2s/2p$ state. Some $3p/3s$–$2s$ antibonding states were found in the energy range from -10 eV to -3 eV for the Si–O_d bond, which somewhat attenuated the interactions of $3p$–$2s$ and $3s$–$2p$ bonding characteristics. Furthermore, a comparison of Al_a–O_b bond (ICOHP = −3.96 eV) interaction strengths and main orbital-pair contribution was also presented in Fig. 6(c). It was observed

12

that Al_a–O_b bond in octahedrons presented weaker bonding interactions in all orbital-pairs compared to Al_b–O_d and Si–O_d bonds in tetrahedrons, which resulted in lower structural stability of octahedral sheet rather than tetrahedral sheet.

4. Conclusion

In the present study, the atomic structure of a typical *trans*-vacant 1*M* Al-rich illite was constructed and systematically investigated with the DFT method. The calculated structural parameters were in good agreement with the available experimental value. The calculated indirect band gap of Al-rich illite was 4.99 eV and as a result it can be treated as an insulator. The bond length analyses indicated that the interactions in tetrahedron sheet were more stable than those in octahedral sheet. The ICOHP values of the Si–O bond and Al–O bond in tetrahedron sheet were −8.36 eV and −5.83 eV, respectively, which revealed the substitutions of Al atoms reduced the stability of tetrahedral sheet. The electronic charge density implied a mixed ionic/covalent bonding property in Al-rich illite. The present findings served as a useful reference to employ the experimental and theoretical investigations in illite mineralogical study.

Acknowledgments

References

Beermann, T. & Brockamp, O. (2005) Structure analysis of montmorillonite crystallites by convergent-beam electron diffraction. *Clay Minerals*, **40**, 1-13.

Bergaya, F. & Lagaly, G. (2013) *Handbook of clay science*. Newnes.

Blöchl, P.E. (1994) Projector augmented-wave method. *Physical Review B*, **50**, 17953-17979.

Bridgeman, C.H. (1996) Ab-initio total energy study of uncharged 2:1 clays and their interaction with water. *Molecular Physics*, **89**, 879-888.

Brigatti, M.F. & Guggenheim, S. (2002) Mica crystal chemistry and the influence of pressure, temperature, and solid solution on atomistic models. *Reviews in Mineralogy and Geochemistry*, **46**, 1-97.

Drits, V.A. & McCarty, D.K. (2007) The nature of structure-bonded h2o in illite and leucophyllite from dehydration and dehydroxylation experiments. *Clays and Clay Minerals*, **55**, 45-58.

Drits, V.A., McCarty, D.K. & Derkowski, A. (2012) Mixed-layered structure formation during trans-vacant al-rich illite partial dehydroxylation. *American Mineralogist*, **97**, 1922-1938.

Drits, V.A., McCarty, D.K. & Zviagina, B.B. (2006) Crystal-chemical factors responsible for the distribution of octahedral cations over trans- and cis-sites in dioctahedral 2:1 layer silicates. *Clays and Clay Minerals*, **54**, 131-152.

Drits, V.A., Zviagina, B.B., McCarty, D.K. & Salyn, A.L. (2010) Factors responsible for crystal-chemical variations in the solid solutions from illite to aluminoceladonite and from glauconite to celadonite. *American Mineralogist*, **95**, 348-361.

Dronskowski, R. & Bloechl, P.E. (1993) Crystal orbital hamilton populations (cohp): Energy-resolved visualization of chemical bonding in solids based on density-functional calculations. *The Journal of Physical Chemistry*, **97**, 8617-8624.

Eberl, D.D., Srodon, J., Lee, M., Nadeau, P.H. & Northrop, H.R. (1987) Sericite from the silverton caldera, colorado; correlation among structure, composition, origin, and particle thickness. *American Mineralogist*, **72**, 914-934.

El Halim, M., Daoudi, L., El Ouahabi, M. & Fagel, N. (2022) Characterization of clays from the fez area (northern morocco) for potential uses in the ceramics industry. *Clay Minerals*, **57**, 139-149.

Ertural, C., Steinberg, S. & Dronskowski, R. (2019) Development of a robust tool to extract mulliken and löwdin charges from plane waves and its application to solid-state

materials. *RSC Advances*, **9**, 29821-29830.

Escamilla-Roa, E., Nieto, F. & Sainz-Díaz, C.I. (2016) Stability of the hydronium cation in the structure of illite. *Clays and Clay Minerals*, **64**, 413-424.

Feng, X., Faiia, A.M., WoldeGabriel, G., Aronson, J.L., Poage, M.A. & Chamberlain, C.P. (1999) Oxygen isotope studies of illite/smectite and clinoptilolite from yucca mountain: Implications for paleohydrologic conditions. *Earth and Planetary Science Letters*, **171**, 95-106.

Geatches, D.L. & Wilcox, J. (2014) Ab initio investigations of dioctahedral interlayer-deficient mica: Modelling 1 m polymorphs of illite found within gas shale. *European Journal of Mineralogy*, **26**, 127-144.

Grim, R.E., Bray, R.H. & Bradley, W.F. (1937) The mica in argillaceous sediments†. *American Mineralogist*, **22**, 813-829.

He, C., Makovicky, E. & Øsbæck, B. (1995) Thermal stability and pozzolanic activity of calcined illite. *Applied Clay Science*, **9**, 337-354.

He, M.-C., Zhao, J. & Fang, Z.-J. (2012) First-principles study of atomic and electronic structures of kaolinite in soft rock. *Chinese Physics B*, **21**, 039101.

Hughbanks, T. & Hoffmann, R. (1983) Chains of trans-edge-sharing molybdenum octahedra: Metal-metal bonding in extended systems. *Journal of the American Chemical Society*, **105**, 3528-3537.

Koga, T., Kanayama, K., Watanabe, T., Imai, T. & Thakkar, A.J. (2000) Analytical hartree–fock wave functions for the atoms cs to lr. *Theoretical Chemistry Accounts*, **104**, 411-413.

Kresse, G. & Furthmüller, J. (1996) Efficient iterative schemes for ab initio total-energy calculations using a plane-wave basis set. *Physical Review B*, **54**, 11169.

Kresse, G. & Joubert, D. (1999) From ultrasoft pseudopotentials to the projector augmented-wave method. *Physical Review B*, **59**, 1758.

Li, H., Ou, J., Wang, X., Yan, Z. & Zhou, Y. (2018) Immobilization of soil cadmium using combined amendments of illite/smectite clay with bone chars. *Environmental Science and Pollution Research*, **25**, 20723-20731.

Maintz, S., Deringer, V.L., Tchougréeff, A.L. & Dronskowski, R. (2016) Lobster: A tool to extract chemical bonding from plane-wave based dft. *Journal of Computational Chemistry*, **37**, 1030-1035.

Mercier, P.H.J., Le Page, Y. & Desgreniers, S. (2010) Kaolin polytypes revisited ab initio at 10 gpa. *American Mineralogist*, **95**, 1117-1120.

Meunier, A. & Velde, B. (2004) The mineralogy of illite — what is illite? Pp. 3-62. In A. Meunier, and B. Velde, Eds. *Illite: Origins, evolution and metamorphism*,Springer Berlin Heidelberg, Berlin, Heidelberg.

Militzer, B., Wenk, H.-R., Stackhouse, S. & Stixrude, L. (2011) First-principles calculation of the elastic moduli of sheet silicates and their application to shale anisotropy.

16

American Mineralogist, **96**, 125-137.

Moellmann, J. & Grimme, S. (2014) Dft-d3 study of some molecular crystals. *The Journal of Physical Chemistry C*, **118**, 7615-7621.

Monkhorst, H.J. & Pack, J.D. (1976) Special points for brillouin-zone integrations. *Physical Review B*, **13**, 5188-5192.

Perdew, J.P., Burke, K. & Ernzerhof, M. (1996) Generalized gradient approximation made simple. *Physical Review Letters*, **77**, 3865-3868.

Rieder, M., Cavazzini, G., D'yakonov, Y.S., Frank-Kamenetskii, V.A., Gottardi, G., Guggenheim, S., Koval', P.W., Müller, G., Neiva, A.M.R., Radoslovich, E.W., Robert, J.-L., Sassi, F.P., Takeda, H., Weiss, Z. & Wones, D.R. (1998) Nomenclature of the micas. *Clays and Clay Minerals*, **46**, 586-595.

Righi, D. & Meunier, A. (1995) Origin of clays by rock weathering and soil formation. Pp. 43-161. In B. Velde, Ed. *Origin and mineralogy of clays: Clays and the environment*, Springer Berlin Heidelberg, Berlin, Heidelberg.

Ruiz Pestana, L., Kolluri, K., Head-Gordon, T. & Lammers, L.N. (2017) Direct exchange mechanism for interlayer ions in non-swelling clays. *Environmental Science & Technology*, **51**, 393-400.

Sánchez-Coronilla, A., Martín, E.I., Fernández-de-Cordova, F.J., Santos, F.J. & Toledo, J.H. (2019) A theoretical study on the inclusion of fe, cu, and zn in illite clays. *Journal of Nanomaterials*, **2019**, 4546350.

Scholtzová, E. & Tunega, D. (2019) Density functional theory study of the stability of the tetrabutylphosphonium and tetrabutylammonium montmorillonites. *Clay Minerals*, **54**, 41-48.

Sedmale, G., Randers, M., Rundans, M. & Seglins, V. (2017) Application of differently treated illite and illite clay samples for the development of ceramics. *Applied Clay Science*, **146**, 397-403.

Shoval, S. (2023) Characterization of the clayey sediments in the environment of exposed mudflats on the western dead sea shore. *Clay Minerals*, 1-39.

Steiger, R.P. (1982) Fundamentals and use of potassium/polymer drilling fluids to minimize drilling and completion problems associated with hydratable clays. *Journal of Petroleum Technology*, **34**, 1661-1670.

Stixrude, L. & Peacor, D.R. (2002) First-principles study of illite–smectite and implications for clay mineral systems. *Nature*, **420**, 165-168.

Teich-McGoldrick, S.L., Greathouse, J.A. & Cygan, R.T. (2012) Molecular dynamics simulations of structural and mechanical properties of muscovite: Pressure and temperature effects. *The Journal of Physical Chemistry C*, **116**, 15099-15107.

Yuan, R., Wang, W.-M., He, Y., Fang, Y. & Huang, X.-L. (2022) Molecular dynamics modelling of na-montmorillonite subjected to uniaxial compression and unidirectional shearing. *Clay Minerals*, **57**, 241-252.

17

Zhang, J.R., Xu, M.D., Christidis, G.E. & Zhou, C.H. (2020) Clay minerals in drilling fluids: Functions and challenges. *Clay Minerals*, **55**, 1-11.

Zhao, J., Wang, Y.-F., Luan, Z.-L., Cao, Y. & He, M.-C. (2023) Theoretical analysis of the effect of doping with na(i), k(i), mg(ii), ca(ii) and fe(ii) on the electronic and mechanical properties of pyrophyllite. *Clay Minerals*, **58**, 113-120.

Zoeller, M. & Brockamp, O. (1997) 1m-and 2m1-illites: Different minerals and not poly types. *European Journal of Mineralogy*, 821-828.

Zviagina, B.B. & Drits, V.A. (2019) Structural factors affecting the crystal-chemical variability in al-rich k-dioctahedral 2m1 micas. *Clay Minerals*, **54**, 169-179.
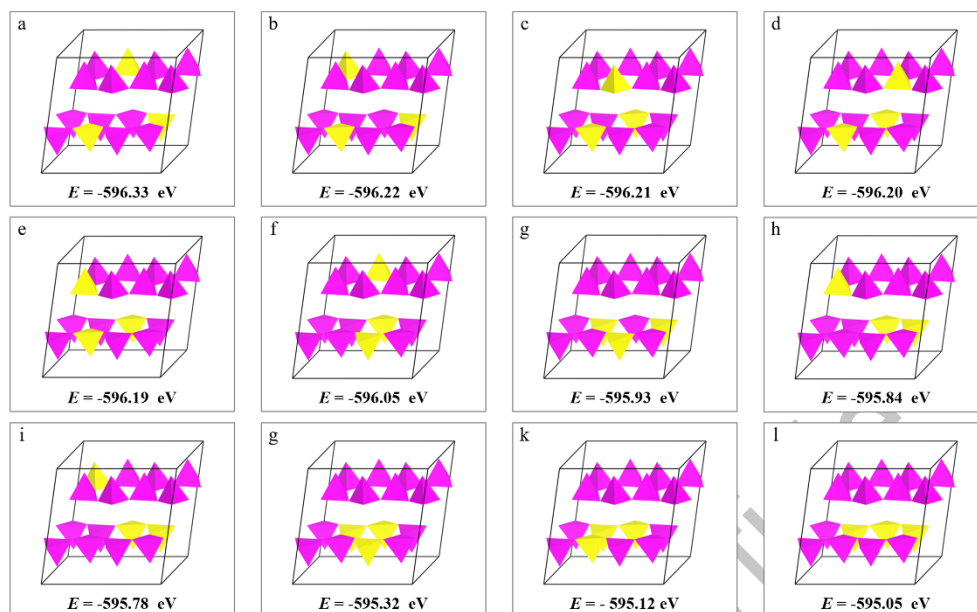
Figure 1. A selection of representative configurations of 13 Si atoms and 3 substituted Al atoms (shown as tetrahedrons) in Al-rich illite unit-cell, arranged in order of energy. Yellow tetrahedrons = Al–O tetrahedrons; pink tetrahedrons = Si–O tetrahedrons.
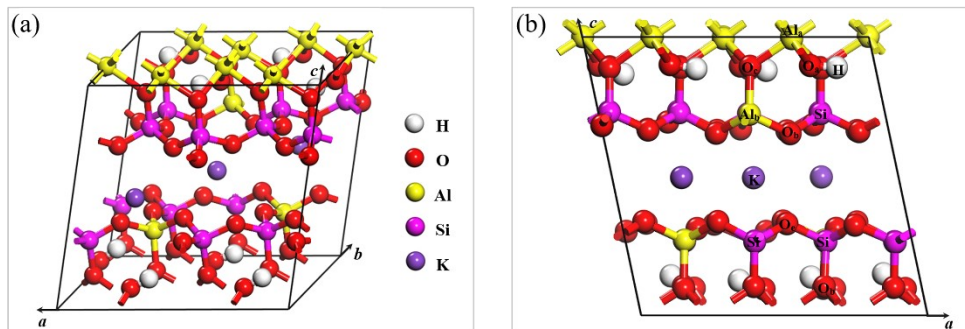
Figure 2. Crystal structures of Al-rich illite $K_3Al_8(Si_{13}Al_3)O_{40}(OH)_8$. (a) Unit cell of Al-rich illite. (b) Characteristic atoms and bonds in Al-rich illite (back view). White spheres = hydrogen; red spheres = oxygen; yellow spheres = aluminum; pink spheres = silicon; and purple spheres = kalium.
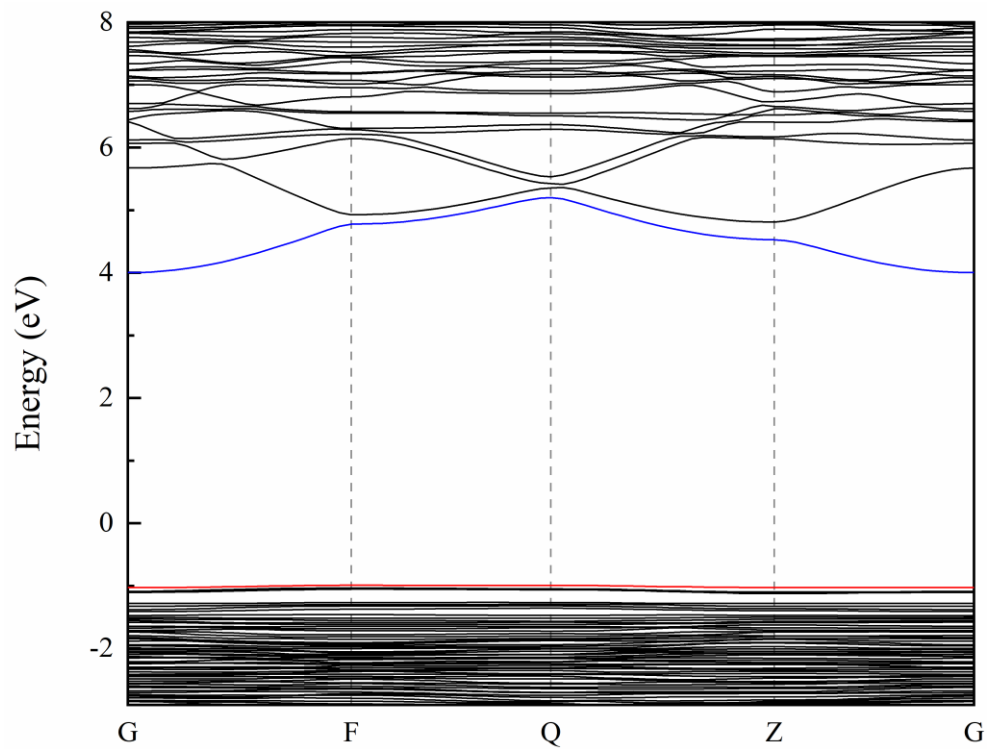
Figure 3. Calculated band structure for Al-rich illite. The red and blue lines represent the

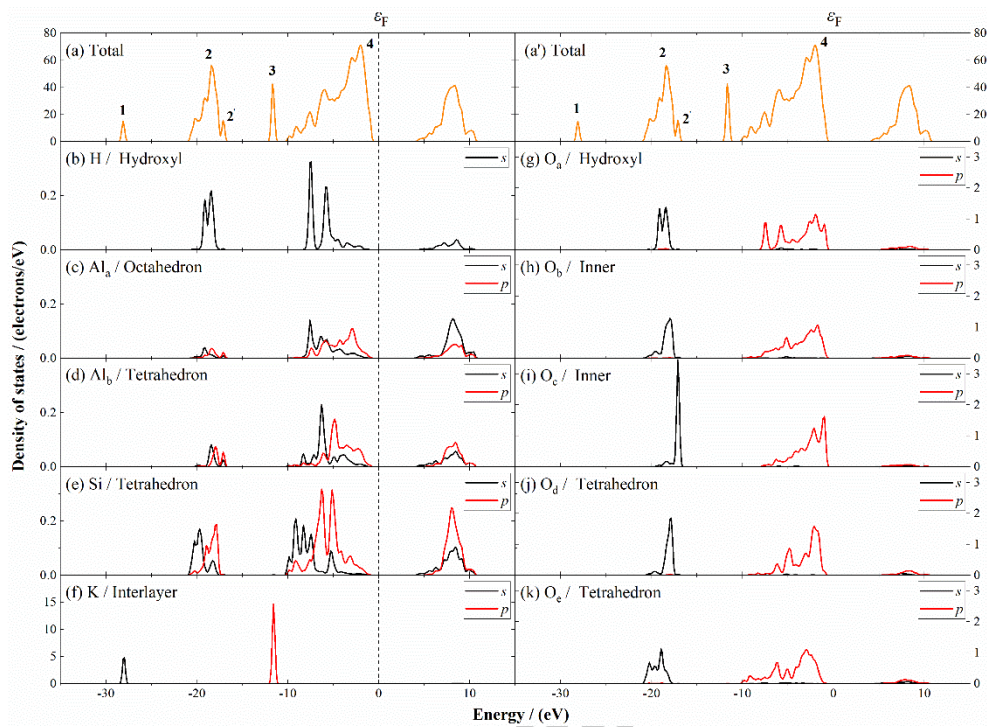bottom of conduction-band and the top of valence-band, respectively.

Figure 4. The calculated electronic total density of state (TDOS) and electronic partial density of state (PDOS) for H, O, Al, Si and K atoms of Al-rich illite.

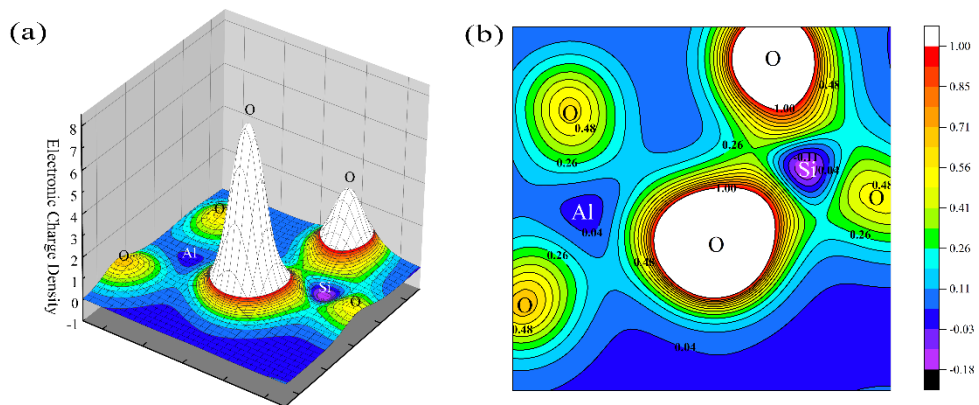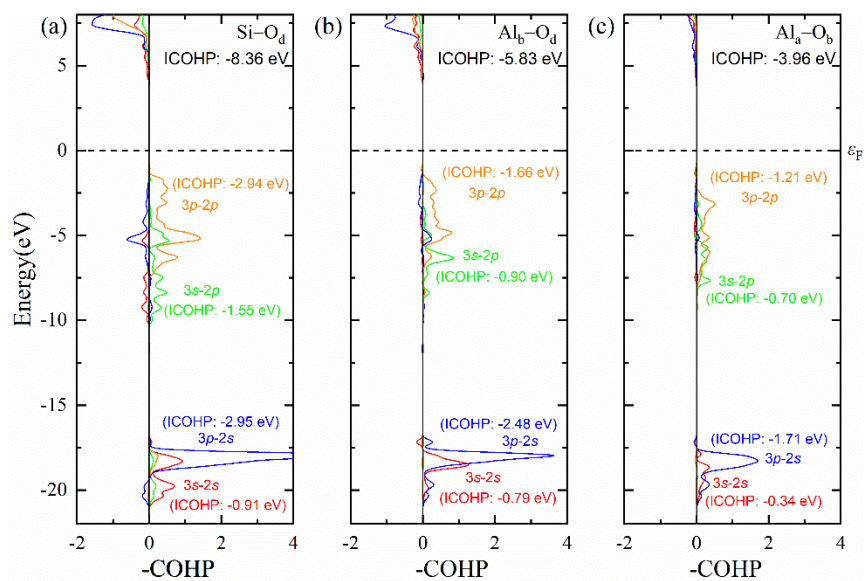**Figure 5**. The sampled 3D & 2D electronic charge density contour plots of Al-rich illite.

Figure 6. The COHP analyses including main orbital-pair contributions for three types of bonds of Al-rich illite: (a) The Si–O$_d$ bond in tetrahedral sheet; (b) The Al$_b$–O$_d$ bond in tetrahedral sheet; (c) The Al$_a$–O$_b$ bond in octahedral sheet.

Table 1. The calculated total energy of the Al-rich illite with different configurations of the 3 substituted tetrahedral Al atoms.

Configuration	Energy/eV	Configuration	Energy/eV
a	**-596.33**	m	-596.21
b	-596.22	n	-596.20
c	-596.21	o	-596.16
d	-596.20	p	-596.16
e	-596.19	q	-596.02
f	-596.05	r	-596.01
g	-595.93	s	-595.98
h	-595.84	t	-595.88
i	-595.78	u	-595.83
j	-595.32	v	-595.80
k	-595.12	w	-595.72
l	-595.05	x	-595.60

Table 2. Calculated and experimental lattice parameters of Al-rich illite.

Phase	$2a$(Å)	b(Å)	c(Å)	α(deg)	β(deg)	γ(deg)
Present	10.455	9.022	10.316	89.94	101.99	89.92
Experimental[1]	10.399	8.982	10.233	90.00	101.60	90.00
Experimental[2]	10.404	8.980	10.227	90.00	101.57	90.00

[1] Eberl et al., 1987.

[2] Drits & McCarty, 2007.

Table 3. Calculated bond length in optimized structure of Al-rich illite.

Bond	H-O_a	Al_a-O_a	Al_a-O_b	Al_a-O_c	Al_b-O_c	Al_b-O_d	Si-O_b	Si-O_d	Si-O_e
Length/Å	0.973	1.928	1.951	1.889	1.752	1.759	1.643	1.607	1.647

Mineralogical Society

Table4. Atomic Mulliken population/charge analysis and COHP bonding analysis for characteristic atoms and bonds in Al-rich illite.

Atom	s	p	total	charge/e	Bond	ICOHP/eV	Length/Å
K	1.99	6.00	7.99	1.01	K—O_d	-0.21	2.80
Al_a	0.49	0.88	1.38	1.62	H—O_b	-8.37	0.97
Al_b	0.44	0.83	1.27	1.73	Al_a—O_a	-4.17	1.93
Si	0.58	1.24	1.82	2.18	Al_a—O_b	-3.96	1.95
H	0.58	0	0.58	0.42	Al_b-O_c	-5.47	1.75
O_a	1.80	5.17	6.96	-0.96	Al_b—O_d	-5.83	1.76
O_b	1.81	5.28	7.09	-1.09	Si—O_b	-7.63	1.64
O_c	1.81	5.32	7.13	-1.13	Si—O_d	-8.36	1.61
O_d	1.82	5.34	7.16	-1.16	Si-O_e	-7.63	1.65
O_e	1.81	5.34	7.15	-1.15			

Table 5. Atomic Mulliken population analysis with specific orbitals for characteristic atoms of Al-rich illite.

Atom	O_a		O_b		O_c		O_d	
	2s	1.80	2s	1.81	2s	1.81	2s	1.82
	2p_y	1.76	2p_y	1.82	2p_y	1.81	2p_y	1.79
Mulliken populations	2p_z	1.82	2p_z	1.71	2p_z	1.77	2p_z	1.80
	2p_x	1.59	2p_x	1.75	2p_x	1.74	2p_x	1.75
	total	6.96	total	7.09	total	7.13	total	7.16
Atom	O_e		Al_a		Al_b		Si	
	2s	1.81	3s	0.49	3s	0.44	3s	0.58
	2p_y	1.79	3p_y	0.30	3p_y	0.28	3p_y	0.43
Mulliken populations	2p_z	1.82	3p_z	0.31	3p_z	0.28	3p_z	0.41
	2p_x	1.73	3p_x	0.27	3p_x	0.27	3p_x	0.40
	total	7.15	total	1.38	total	1.27	total	1.82